Unveiling the microstructure and promising electrochemical performance of heavily phosphorus-doped diamond electrodes

Baluchová, Simona; Sung, Kil dong; Weiss, Zdeněk; Kopeček, Jaromír; Fekete, Ladislav; Buijnsters, Josephus G.; Mortet, Vincent

DOI
10.1016/j.electacta.2024.144696

Publication date
2024

Document Version
Final published version

Published in
Electrochimica Acta

Electrochimica Acta 499 (2024) 144696

Contents lists available at ScienceDirect

Electrochimica Acta

journal homepage: www.journals.elsevier.com/electrochimica-acta

Unveiling the microstructure and promising electrochemical performance of heavily phosphorus-doped diamond electrodes

Simona Baluchová [a,*], Kil-dong Sung [b,*], Zdeněk Weiss [b], Jaromír Kopeček [b], Ladislav Fekete [b], Josephus G. Buijnsters [c], Vincent Mortet [b,d]

[a] Department of Analytical Chemistry, Faculty of Science, Charles University, Albertov 6, 128 00 Prague, Czech Republic
[b] FZU – Institute of Physics of the Czech Academy of Sciences, Na Slovance 1999/2, 182 00 Prague, Czech Republic
[c] Department of Precision and Microsystems Engineering, Faculty of Mechanical Engineering, Delft University of Technology, Mekelweg 2, 2628 CD Delft, the Netherlands
[d] Faculty of Biomedical Engineering, Czech Technical University in Prague, Sítná Sq. 3105, 272 01 Kladno, Czech Republic

ARTICLE INFO

Keywords:
Phosphorus-doped diamond (PDD)
Gas flow control
n-Type conductivity
Electrochemical characterisation
Cyclic voltammetry analysis

ABSTRACT

The challenge of doping synthetic diamond with phosphorus stems from the atomic size mismatch between phosphorus and carbon atoms, which previously hindered achieving high phosphorus doping levels. This limitation delayed the exploration of phosphorus-doped diamond (PDD) in electrochemical applications, where it holds potential as a novel and appealing electrode material because PDD uniquely combines diamond's exceptional properties with phosphorus atoms inducing n-type conductivity. In this study, heavily doped PDD electrodes were successfully developed using chemical vapour deposition, followed by comprehensive microstructural and electrochemical characterisations. The influence of phosphorus doping, manipulated via high phosphine gas concentration or time-dependant precursor gas flow control, on the PDD properties was thoroughly examined. PDD layers grown at higher phosphine concentrations demonstrated enhanced phosphorus incorporation, leading to a higher prevalence of fine nano-crystalline diamond grains and non-diamond carbon components, while also slowing the growth rate. Notably, a distinct PDD sample produced under dynamic gas flow with lower phosphine concentration revealed larger grain sizes, increased effective deposition rate, and improved phosphorus levels compared to its counterpart synthesized under static conditions. Cyclic voltammetry in a 1 mol L^{-1} KCl solution revealed a low double-layer capacitance (<11 μF cm^{-2}) in all as-grown PDD electrodes. However, significant differences between the samples emerged during the experiments conducted with redox probes $[Ru(NH_3)_6]^{3+/2+}$ and $[Fe(CN)_6]^{3-/4-}$. Particularly, higher phosphorus content promoted well-developed voltammograms, significantly reduced peak-to-peak separation values, faster electron transfer rates, and increased peak currents. Furthermore, the possibility of using heavily P-doped diamond electrodes for the detection of two organic analytes, dopamine and ascorbic acid, was successfully manifested. All in all, the as-grown, highly P-doped diamond electrodes proved their ability, first time ever, to record well-defined signals of both inorganic redox probes and complex organic compounds, unravelling their potential in electroanalysis and sensor development and broadening the scope of PDD utilisation.

1. Introduction

The atomic structure of diamond is built up of sp^3-hybridized carbon atoms arranged in a tetrahedral shape and connected with strong covalent bonds, which create a dense crystal lattice. This compact arrangement gives rise to the remarkable properties of diamond such as its extreme mechanical hardness, robustness, high chemical stability, wide band gap (5.48 eV), high thermal conductivity, and high charge carrier mobility [1-3]. On the other hand, this high atomic density makes it very difficult to incorporate different, and particularly larger, atoms into the diamond lattice and only limited number of dopants can be introduced via intentional and controlled doping during the diamond growth process such as chemical vapour deposition (CVD). Boron, nitrogen, and phosphorus belong amongst the available and most widely studied dopants, having ability to substitute carbon atoms in the diamond lattice [1,4].

* Corresponding authors.
E-mail addresses: simona.baluchova@natur.cuni.cz (S. Baluchová), sung@fzu.cz (K.-d. Sung).

https://doi.org/10.1016/j.electacta.2024.144696
Received 21 March 2024; Received in revised form 4 July 2024; Accepted 8 July 2024
Available online 9 July 2024

Boron (B) possesses both a small atomic radius and a relatively low activation energy (0.37 eV) [1], and has a high solubility in diamond. Incorporated boron atoms act as acceptors in the diamond lattice and create a p-type material. Importantly, the combination of the former properties enables a heavy B-doping of diamond. This is effectively used to produce boron-doped diamond (BDD) materials, whose electrical properties can be readily modified, ranging from semiconductive to metal-like conductive. As a result, conductive BDD has become a well-established electrode material with many applications in various electrochemical fields [5], including electroanalysis [6,7], electrooxidation of organic pollutants and waste-water treatment [8,9], electrosynthesis [10], and electro(photo)catalysis [11,12]. The effect of B-doping on the morphological, structural, and electrochemical features of the fabricated BDD electrodes has been extensively examined [6, 13-18].

In contrast to boron, the incorporation of n-type dopants in the diamond lattice is limited and inefficient. Nitrogen is the most prevalent impurity in (natural) diamond due to its abundant presence in the atmosphere (78.1 vol.%) and its atomic size comparable to that of carbon. Although N impurities can act as donors, the fabrication of n-type semiconductor devices using nitrogen-doped diamond (NDD) has been shown to be ineffective [19], mainly due to the very high activation energy of nitrogen (1.7 eV) [1]. Notably, nitrogen in diamond can occur in several forms, including isolated substitutional nitrogen, nitrogen-vacancy (NV), or nitrogen-vacancy-hydrogen (NVH) [4]. Particularly, NV centres have been widely explored for quantum technologies, nanoscale magnetometry, and (bio)sensing applications [19, 20].

Another representative of an n-type dopant is phosphorus (P), possessing lower activation energy (~0.6 eV) than nitrogen [1] but also much larger atomic radius compared to carbon. Consequently, the large P atoms cannot readily substitute carbon atoms in the diamond lattice, despite evidence of substitutional doping with P atoms [21]. Only a few successful attempts can be tracked in the literature reporting on the fabrication of heavily P-doped diamond (PDD) layers (with phosphorus concentrations [P] $>10^{20}$ cm^{-3}), either in single-crystal [22-24] or polycrystalline form [25-27], using higher concentrations of phosphorus precursors during the deposition process. Even fewer studies have focused on the characterisation of the electrochemical properties of PDD films [26,28-30], whose [P], however, have widely ranged from 10^{16} to 10^{20} atoms cm^{-3}. Besides electrochemistry, PDD has been recognized as one of the most notable wide bandgap materials, which is well-suited for the development of high-power electronic devices [31,32], thermionic emission cathodes [25], UV photodetectors [33], and high-frequency transistors [34].

Recently, we have achieved advancements in increasing the phosphorus concentration in polycrystalline PDD by manipulating radical species in the plasma using a time-dependant gas flow technique [27, 35]. The strong interactions between PH and CH radicals in the plasma inevitably creates unwanted species such as methinophosphide (HCP) or methylphosphine (CH_3PH_2) during the PDD growth process. Nevertheless, the formed radical species can be regulated by pulsing methane (CH_4) gas at low phosphine concentration, which was manifested to circumvent interactions between PH and CH radicals and to facilitate effective phosphorus incorporation into the diamond layer by alternating the major radical species in the plasma [35].

In the present study, we aimed to elucidate the microstructural and electrochemical properties of nanocrystalline PDD layers with varying P doping levels (four in total). To obtain heavily doped PDD (hPDD), the layers were synthesized in a chemical vapour deposition (CVD) chamber using high phosphine concentrations. Furthermore, one PDD sample was deposited at a lower phosphine concentration but under dynamic gas flow conditions to assess the impact of gas flow techniques on the material's final characteristics. The phosphorus concentration in the various PDD layers was probed by glow discharge optical emission spectroscopy (GDOES), while scanning electron microscopy (SEM) and Raman spectroscopy were employed for morphological and chemical analysis of the PDD layers. Cyclic voltammetry (CV) measurements were conducted to determine valuable electrochemical characteristics such as double-layer capacitance (C_{dl}) and peak-to-peak separation (ΔE_p) values indicative of the electron transfer rates. Lastly, the nanocrystalline PDD samples were subjected to CV experiments with structurally more complex, redox-active organic molecules, specifically dopamine and ascorbic acid (vitamin C), to demonstrate their perspective use as a promising electrode material in electroanalytical and sensing applications.

2. Experimental

2.1. Chemicals

Analytical grade chemicals were acquired from Merck and used as-received: potassium chloride (≥ 99%), sulfuric acid (97%), phosphate buffered saline (PBS, tablets, 10 mM, pH 7.4), hexaammineruthenium(III) chloride (≥ 98%), potassium hexacyanoferrate(II) trihydrate (≥ 98.5%), l-ascorbic acid (≥ 99%), dopamine hydrochloride (≥ 98%), isopropanol, acetone. Deionized (DI) water with a resistivity of >18.0 MΩ cm, purified with a LWTN Genie A system (Laboratorium Water Technologie Nederland), was used to prepare all aqueous solutions and for ultrasonic cleaning.

2.2. Growth of P-doped diamond layers

Conductive Si substrates (10×10 mm^2) were cleaned using acetone and isopropanol in an ultrasonic bath for 10 min. Subsequently, a nanoparticle diamond seed solution was uniformly distributed onto the substrate surfaces using a spin coater to establish diamond nucleation sites. PDD layers were grown using a lab-made NIRIM type microwave plasma-enhanced chemical vapour deposition (MWPECVD) system [27, 35]. The chamber was initially evacuated to reach a base pressure $<10^{-6}$ mbar, and the working pressure was regulated to 80 mbar using a flow MKS control valve. Plasma was ignited by delivering microwave power at 0.45 kW and a frequency of 2.45 GHz from a GMP 30 K microwave generator (Sairem, France) to the downstream via a WR340 waveguide. The substrate was positioned into the reactor to reach a temperature of ca 1000 °C, ensuring optimal conditions for the deposition process. PH_3 (N5.0, diluted at 6000 ppm in H_2), CH_4 (N5.5), and H_2 (N5.6) gases were used to grow the PDD layers. The total gas flow rate was set at 1000 sccm using GE50A mass flow controllers (MKS, USA). Precise control of individual gas flow rates was achieved through a homemade LabVIEW program, enabling static and dynamic gas flows. For static gas flow, the concentration of CH_4 in H_2 ($[CH_4]/[H_2]$) was maintained at 0.4%, while the concentration of PH_3 in H_2 ($[PH_3]/[H_2]$) varied logarithmically as 63, 250, and 1000 ppm, resulting in concentration ratios of PH_3 to CH_4 ($[PH_3]/[CH_4]$) of 16k, 63k, and 250k ppm, respectively. On the other hand, dynamic gas flow control involved the linear increase and decrease of $[CH_4]/[H_2]$ from 0 to 0.4% within a 30 second cycle at a constant $[PH_3]/[H_2]$ of 63 ppm. Note that the effect of time-dependant CH_4 control reversed as $[PH_3]/[H_2]$ increased, due to the remnant PH radicals at high $[PH_3]/[CH_4]$ and difficulties in changing radical species during the dynamic gas flow [35] (Fig. S1). Deposition time for static gas flow was 2 h, while it was extended to 3 h for dynamic gas flow to compensate for the lower total amount of $[CH_4]/[H_2]$. The as-prepared PDD samples deposited under static gas flow will be labelled from here onwards as PDD-63, PDD-250, and PDD-1000, whereas PDD-63-D will denote the only sample grown using dynamic gas flow (the numbers used in the labelling correspond to the $[PH_3]/[H_2]$ ratios used during the deposition process). Finally, an undoped diamond layer, used for comparison purposes, was grown in another NIRIM type reactor to prevent any potential unwanted doping from internal reactor contamination.

2.3. Chemical, morphological, and structural characterisation

Phosphorus concentrations ([P]) were measured by glow discharge optical emission spectroscopy (GDOES) using the GDA750HR spectrometer (Spectruma, Germany). This apparatus was equipped with a 2.5 mm internal anode Grimm-type spectral source and operated with a dc discharge in argon at 850 V/15 mA. Quantitative depth profiles of the P-doped diamond layers were established based on a multi-matrix calibration by bulk reference materials with certified concentrations of phosphorus, carbon, and other elements [36,37], exhibiting no matrix effects, virtually no hydrogen present, and negligible self-absorption. Sputter rate-corrected calibration was performed with proper certified reference materials, in accordance with the EN/ISO standard 17025. For phosphorus analysis, the emission intensity of the P I, 178.284 nm line was collected. The precision of the resulting phosphorus concentration is constrained by spectral background at this wavelength [37,38], which primarily stems from a nearby Ar II line at 178.259 nm and exhibits slight variations, not related to the phosphorus content. The background at $\lambda = 178.284$ nm can be substantially suppressed and the precision at low phosphorus concentrations thereby improved by using neon as the discharge gas instead of argon [37]. The [P] incorporated at high $[PH_3]/[H_2]$ shows comparable values to those obtained using the secondary ion mass spectrometry (SIMS) technique [35], confirming the accuracy and reliability of the GDOES measurements for determining phosphorus concentrations in hPDD layers.

For further investigation, an inVia Raman spectroscope (Renishaw, UK) was employed, using an excitation laser at a wavelength of 488 nm. The obtained Raman spectra of the grown diamond layers were baseline subtracted and fitted using Gaussian peaks for accurate peak analysis. Information regarding peak position (ω), intensity (I), and full width at half maximum (FWHM) of each peak was collected for subsequent analysis. Wide-range Raman spectra from 300 to 3000 cm^{-1} were obtained using 488 nm and 514 nm lasers to identify phosphorus-related peaks (see Fig. S2).

To observe the surface morphologies of the various diamond layers, a scanning electron microscope (SEM) FERA3 GM (Tescan, Czech Republic) with a relatively low acceleration voltage (2.0 kV) was employed to minimize charging effects. Layer thickness of each sample was determined by analysing the line profile of the height differences between seeded and unseeded areas using an atomic force microscope (AFM) Dimension Icon (Bruker, USA) in a peak force tapping mode with ScanAsyst Air tips (Bruker; k: 0.4 N m^{-1}, nominal tip radius: 2 nm).

2.4. Electrochemical measurements

The electrochemical measurements were conducted at laboratory temperature (23 ± 1 °C) using an Autolab PGSTAT128N equipped with the FRA module and controlled by Nova 2.1 software (Metrohm, the Netherlands). The PDD samples, used as the working electrodes, were mounted in a lab-made Teflon electrochemical cell from underneath and the electrode surface area exposed to the solution ($A_{geom} = 0.20$ cm^2) was defined by a circular aperture of 5 mm. A standard three-electrode arrangement was then completed with a silver-silver chloride electrode (Ag|AgCl|3 mol L^{-1} NaCl; Bio-Logic, France) and a coiled 23 cm platinum wire (with a surface area of ~3.6 cm^2; Bio-Logic, France), which served as the reference and auxiliary electrodes, respectively. The PDD samples were examined only in their 'as-deposited' state and no intentional pretreatment, either thermal or electrochemical, was applied prior to the measurements. The electrodes were only sonicated in a series of solvents, particularly acetone, isopropanol, and deionized water, each for 5 min.

Cyclic voltammograms were measured from lower to higher potential values and backwards, typically using a scan rate (v) of 0.10 V s^{-1}, if not stated otherwise, for the following solutions: supporting electrolytes (1 mol L^{-1} KCl, 0.1 mol L^{-1} H_2SO_4, 10 mmol L^{-1} PBS of pH 7.4), redox probes $[Ru(NH_3)_6]^{3+/2+}$ and $[Fe(CN)_6]^{3-/4-}$ (both 1 mmol L^{-1} in 1 mol L^{-1} KCl), and two organic analytes

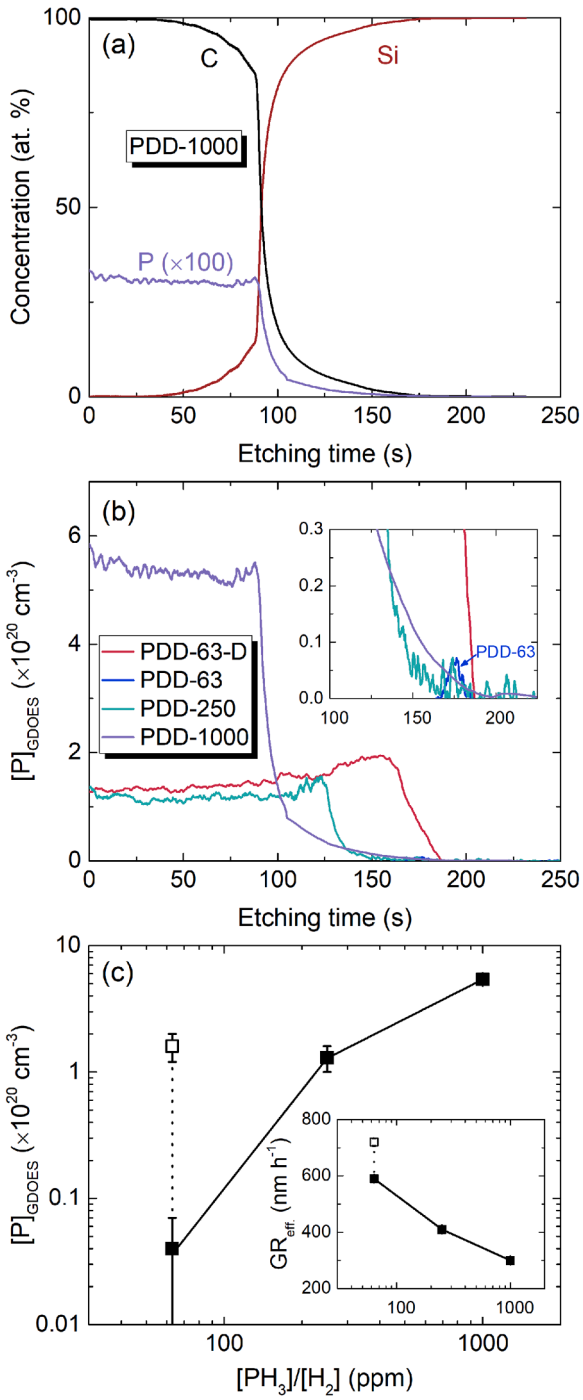

Fig. 1. (a) GDOES depth profile for atomic concentrations of phosphorus (P), carbon (C), and silicon (Si) of the PDD-1000 layer grown using the static gas flow. Note that the concentration of P is magnified 100× for visibility. (b) Etching time-dependant phosphorus concentrations ($[P]_{GDOES}$) for PDD layers. In the inset, magnified depth profiles near the interfaces of PDD layer and substrate are displayed. (c) Phosphorus concentration for layers grown at different $[PH_3]/[H_2]$ using static (closed squares with solid line) and dynamic (open square with dotted line) gas flows. In the inset, the effective growth rate (GR_{eff}) is plotted against $[PH_3]/[H_2]$ ratios for the layers grown using static (closed squares with solid line) and dynamic (open square with dotted line) gas flows.

Table 1
An overview of the fabricated and characterised PDD layers with listed growth conditions and characteristics of each PDD layer.

Sample	$[PH_3]/[H_2]$ (ppm)	Gas flow	T (nm)	GR_{eff} (nm h^{-1})	$[P]_{GDOES}$ ($\times 10^{20}$, cm^{-3})	$[P]_{MS}$ ($\times 10^{20}$, cm^{-3})	C_{dl} ($\mu F\ cm^{-2}$)
PDD-63-D	63	Dynamic	1080 ± 20	720 ± 13	1.6 ± 0.4	0.12 ± 0.08	11.1 ± 0.5
PDD-63	63	Static	1180 ± 20	590 ± 10	0.04 ± 0.03	0.002 ± 0.001	6.1 ± 0.3
PDD-250	250	Static	820 ± 15	410 ± 8	1.3 ± 0.3	0.84 ± 0.25	3.7 ± 0.5
PDD-1000	1000	Static	600 ± 15	300 ± 8	5.4 ± 0.4	2.1 ± 0.3	3.9 ± 0.4

dopamine (100 μmol L^{-1} in 10 mmol L^{-1} PBS of pH 7.4) and ascorbic acid (100 μmol L^{-1} in 0.1 mol L^{-1} H_2SO_4). In addition, CVs recorded in a 1 mol L^{-1} KCl solution in the potential range from −0.2 V to +0.2 V were used for the estimation of double-layer capacitance (C_{dl}) using the equation (Eq. (1)) [3]:

$$C_{dl} = \Delta I_{AV}/A_{geom}\nu \quad \text{(Eq. 1)}$$

where ΔI_{AV} represents the average background current difference (in A) between the forward and backward scan at a potential of 0 V, A_{geom} is the exposed surface area of the PDD working electrode (0.20 cm^2), and ν stands for the applied scan rate (0.10 V s^{-1}).

The Mott-Schottky (MS) analysis was performed in a solution of 1 mol L^{-1} KCl in the potential range from −0.4 V to +1.5 V at a frequency of 10 Hz. Subsequently, the slope of the linear part of each MS plot was identified and applied in the Mott-Schottky equation (Eq. (2)) to estimate the donor concentration (N_D) [28], which is later in the text denoted as $[P]_{MS}$:

$$N_D(\sim [P]_{MS}) = 2/\left(e\varepsilon_0\varepsilon_r A^2\left[d\left(C_p^{-2}\right)/dE\right]\right) \quad \text{(Eq. 2)}$$

where e is an elementary charge (1.602×10^{-19} C), ε_0 is the permittivity of vacuum (8.854×10^{-12} C V^{-1} m^{-1}), ε_r is the relative permittivity of diamond material (5.8), A is the electrode area (2.0×10^{-5} m^2), and C_p (F) is the capacitance obtained at various potential values E (V).

3. Results and discussion

3.1. GDOES analysis

3.1.1. Phosphorus concentration in the PDD layers

Fig. 1(a) shows the GDOES depth profile of phosphorus, carbon and silicon in the PDD-1000 layer. As phosphine gas was introduced during the diamond deposition process, the depth profile of phosphorus exhibits a similar trend to that of carbon. In Fig. 1(b), an overlay of phosphorus depth profiles measured by GDOES ($[P]_{GDOES}$) in different layers are plotted for comparison. Note that the depth profile of the PDD-63 approached the detection limit (~1.0×10^{18} cm^{-3}) of the GDOES analysis of phosphorus across the layer, with a slight increase at the interface, reaching $[P]_{GDOES} = 7.0 \times 10^{18}$ cm^{-3}. As a result, the respective $[P]_{GDOES}$ profile is hardly distinguished in Fig. 1(b). In Fig. 1 (c), the averaged $[P]_{GDOES}$ (listed in Table 1) are plotted for PDD-63, PDD-250, and PDD-1000 as function of the PH_3 concentrations in the gas phase, and, as expected, $[P]_{GDOES}$ increased with the rising $[PH_3]/[H_2]$ ratios in the gas phase and reached a maximum value of 5.4×10^{20} cm^{-3} for the PDD-1000 sample, nearly equivalent to the highest reported value of ~7×10^{20} cm^{-3} [27,35].

Compared to the static gas flow, the PDD-63-D layer grown using the dynamic gas flow demonstrated a remarkable enhancement in $[P]_{GDOES}$ as shown in Fig. 1(b) and 1(c). This substantial increase in $[P]_{GDOES}$ indicates a significant effect of dynamic gas flow on the phosphorus incorporation. It is well established that CH_4 strongly interacts with PH radicals in the plasma, inhibiting the incorporation of phosphorus atoms into the diamond layers [35,39]. However, the decreased amount of CH_4 during the dynamic gas flow process leads to the observed increase in PH radicals, resulting in enhanced phosphorus incorporation in the layers [35]. Although a longer duration is required for the residual CH radicals to flow out of the reaction chamber after discontinuing CH_4 gas, a 30 second period for ascending and descending gas flows effectively controls most CH radicals in the plasma under the growth conditions of a total flow rate of 1000 sccm and a pressure of 80 mbar [40]. Consequently, the dynamic gas flow process enables a higher incorporation of PH radicals into the diamond layer compared to the static gas flow conditions.

3.1.2. Growth rate of the PDD layers

The abrupt drop in phosphorus concentration observed in Fig. 1(a) and (b), coinciding with the abrupt increase in silicon concentration, provides a marker for the layer-substrate interface and correlates proportionally with the diamond layer thickness. To calculate the effective growth rate (GR_{eff}), etching times established from GDOES depth profiles were converted into thicknesses by correlating them with the actual layer thicknesses obtained from AFM results (overviewed in Table 1). The relationship between thickness (T) and etching time (t) is determined using the equation (Eq. (3)):

$$T(\text{nm}) = 6.3(\text{nm s}^{-1}) \times t(\text{s}) \quad \text{(Eq. 3)}$$

The GR_{eff} for different $[PH_3]/[H_2]$ is plotted in the inset of Fig. 1(c) and tabulated in Table 1. Note that the deposition time for the layers using the static gas flow is 2 h, whereas for the layer using dynamic gas flow, it extends to 3 h to compensate for the lower total CH_4 flow. As the $[PH_3]/[H_2]$ ratio increased, the growth rate reduced dramatically because the increased amount of PH radicals interacts with more CH radicals, consequently limiting the available source for diamond growth. Similarly, the dynamic gas flow seems to reduce the growth rate significantly. However, the dynamic gas flow consumes half the amount of CH_4 compared to the static gas flow during the growth process. Therefore, considering the total injected CH_4 flow within the deposition time, GR_{eff} of the PDD-63-D sample grown using the dynamic gas flow (720 ± 13 nm h^{-1}) is higher than the PDD-63 sample grown using the static gas flow (590 ± 10 nm h^{-1}).

3.2. Raman spectroscopy and scanning electron microscopy

3.2.1. Diamond peak analysis

In Fig. 2(a), the Raman spectrum of a PDD-63 sample is presented, providing a detailed analysis for a deeper understanding of the layer composition (spectra of the remaining samples were also deconvoluted and are depicted in Fig. S3). Given that polycrystalline diamond layers consist of diamond grains and other carbon components, the Raman spectra can be decomposed into six peaks [41]: *trans*-polyacetylene (*t-PA*$_1$: ~1150 cm^{-1}; *t-PA*$_2$: ~1480 cm^{-1}), nanocrystalline diamond (d_{nc}: ~1200–1250 cm^{-1}), diamond (d: ~1332 cm^{-1}), and amorphous carbon (G: ~1600 cm^{-1}; D: ~1350 cm^{-1}). To elucidate the relationship between [P] in the layer and the diamond properties, the peak position (ω_d) and the full width at half maximum ($FWHM_d$) of the d peaks are plotted against $[P]_{GDOES}$ in Fig. 2(b). Well-matched linear fitting of ω_d and $FWHM_d$ reveals that the positioning of the diamond peak significantly correlates with the phosphorus concentration present in the layer. As $[P]_{GDOES}$ increases, ω_d shifts towards lower wavenumbers, which is accompanied by an increase in $FWHM_d$ for layers grown using the static gas flow. This linearity also coincides with the layer grown using the dynamic gas flow, i.e., a red shift and broadening of diamond

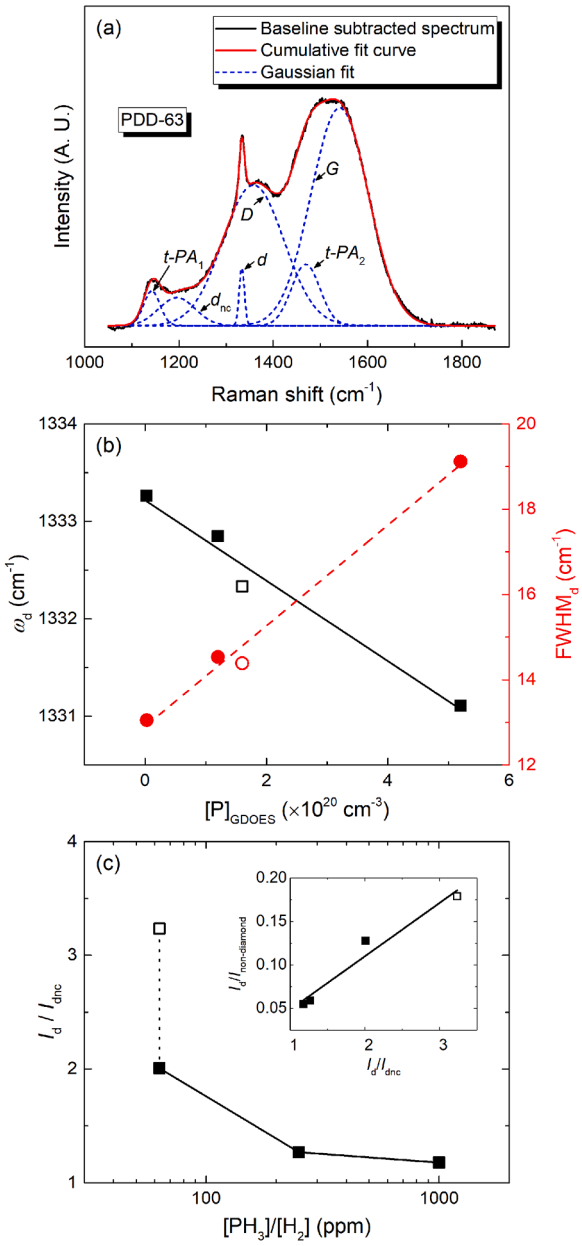

Fig. 2. (a) Baseline subtracted Raman spectrum of the PDD-63 sample (black line), deconvoluted Gaussian peaks (blue dashed lines) contributed from *trans*-polyacetylene (*t-PA*$_1$ and *t-PA*$_2$), nanocrystalline diamond (d_{nc}), diamond (*d*), and amorphous carbon (*G* and *D*), and the cumulative curves of the Gaussian peaks (red line). (b) Raman shift (ω_d: black squares, left y-axis) and full width at half maximum (FWHM$_d$: red circles, right y-axis) of the diamond peak plotted against [P]$_{GDOES}$ for the layers grown using static (closed symbols) and dynamic gas flow (open symbols). Linear fitting of ω_d (black solid line) and FWHM$_d$ (red dotted line) for [P]$_{GDOES}$ is also presented. (c) The intensity ratio of diamond to nanocrystalline diamond peaks (I_d/I_{dnc}) for layers grown at different [PH$_3$]/[H$_2$] using static (closed squares with solid line) and dynamic (open square with dotted line) gas flows. In the inset, the intensity ratio of diamond to the sum of non-diamond peaks ($I_d/I_{non\text{-}diamond}$) is plotted against ($I_d/I_{dnc}$) for the layers grown using static (closed squares) and dynamic (open square) gas flows with the linear fitting (solid line).

peaks compared to the layers grown using the static gas flow. Recent analyses in single-crystalline BDD layers through Raman spectroscopy emphasize the close relationship between dopant ratios and diamond peak properties [42,43]. This correlation is attributed to electronic Raman scattering and multiple Fano functions, related to the carrier concentration and carrier mobility of the layer. Despite the lack of Raman spectroscopy studies on PDD layers, the observed variations of ω_d and FWHM$_d$ in the herein studied PDD layers indicate increased strain at high [P] with structural degradation. This is likely related to the incorporation of phosphorus atoms in the diamond lattice, rather than being only simply present as components of non-diamond carbon compounds [21,44]. Moreover, the broad and low-intensity peak observed below 1000 cm^{-1}, especially under a 514 nm excitation laser, also suggests a high concentration of phosphorus atoms in diamond layers, particularly in PDD-250 and PDD-1000 (see Fig. S2) [45]. Although the precise atomic configurations remain unclear, it is hypothesized that the combination of carbon, phosphorus, and vacancies might also significantly contribute to the observed shifts and broadening of the diamond peaks [46].

3.2.2. *Diamond microstructures*

In Fig. 2(c), the intensity ratio of diamond to nanocrystalline diamond peaks (I_d/I_{dnc}) is plotted for the layers grown at different [PH$_3$]/[H$_2$], showing decreasing trends as [PH$_3$]/[H$_2$] increases. Additionally, the increased I_d/I_{dnc} is accompanied by an increased intensity ratio of diamond to the sum of non-diamond peaks ($I_d/I_{non\text{-}diamond}$). The higher amount of nanocrystalline diamond grains in the PDD layers grown at higher [PH$_3$]/[H$_2$] significantly amplified the area of grain boundaries and the amount of non-diamond carbon components in the layer, resulting in lower $I_d/I_{non\text{-}diamond}$ and I_d/I_{dnc}. This trend aligns closely with the observed surface morphology in the SEM results as shown in Fig. 3. Compared to undoped polycrystalline diamond layers characterised by grains exceeding 100 nm in diameter with facet planes (see Fig. S4(e)), the PDD layers showed smaller grain sizes (less than 100 nm in diameter) with rounded shapes. Moreover, the average grain size of the diamond further decreased with an increase in [PH$_3$]/[H$_2$]. This correlation between Raman spectroscopy and SEM results indicates that PH$_3$ addition led to a reduction in the size of the diamond grains.

The PDD layer grown using the dynamic gas flow exhibited a larger average diamond grain size and a lower amount of non-diamond constituents in the layer. An intriguing observation is that the layer grown with the dynamic gas flow demonstrated two distinct properties in surface morphology and phosphorus concentration compared to the layer grown using static gas flow. In the static gas flow, higher [PH$_3$]/[H$_2$] is necessary to enhance phosphorus incorporation in the layer, but this leads to a reduction in grain size and deposition rate. On the other hand, the dynamic gas flow method provides larger grain sizes, higher effective deposition rate, and improved phosphorus concentration. Further investigation is required, but it appears that during the dynamic gas flow process, diamond growth is predominantly influenced by stages where CH$_4$ flow is high, while phosphorus doping is governed by stages where CH$_4$ flow is low (and PH$_3$ flow is high). This suggests the possibility of managing grain sizes and phosphorus concentrations simultaneously by controlling the CH$_4$ flow.

3.3. *Electrochemical characterisation in a supporting electrolyte*

3.3.1. *Cyclic voltammetric measurements*

The PDD samples were subjected to electrochemical measurements in their as-prepared state, i.e., without any thermal nor electrochemical pre-treatment. First, cyclic voltammograms (CVs) in a supporting electrolyte solution of 1 mol L^{-1} KCl were recorded within a short potential range from −0.2 V to +0.2 V where only background (non-faradaic) currents flow, as shown in Fig. S5. These measurements served to determine the double-layer capacitance (C_{dl}) values (see Eq. (1)), which are listed in Table 1. The three PDD samples prepared with a static growth mode provided a quasi-rectangular shape of the CVs and similarly low C_{dl} values in the range of 3.7 – 6.1 μF cm^{-2}. A slightly higher C_{dl} of 11.1 μF cm^{-2} was assessed for the PDD-63-D sample, grown using the dynamic gas flow mode. The acquired values are well in line with a previous study on a hPDD sample (with [P] of 5 × 10^{20} cm^{-3}) in which a

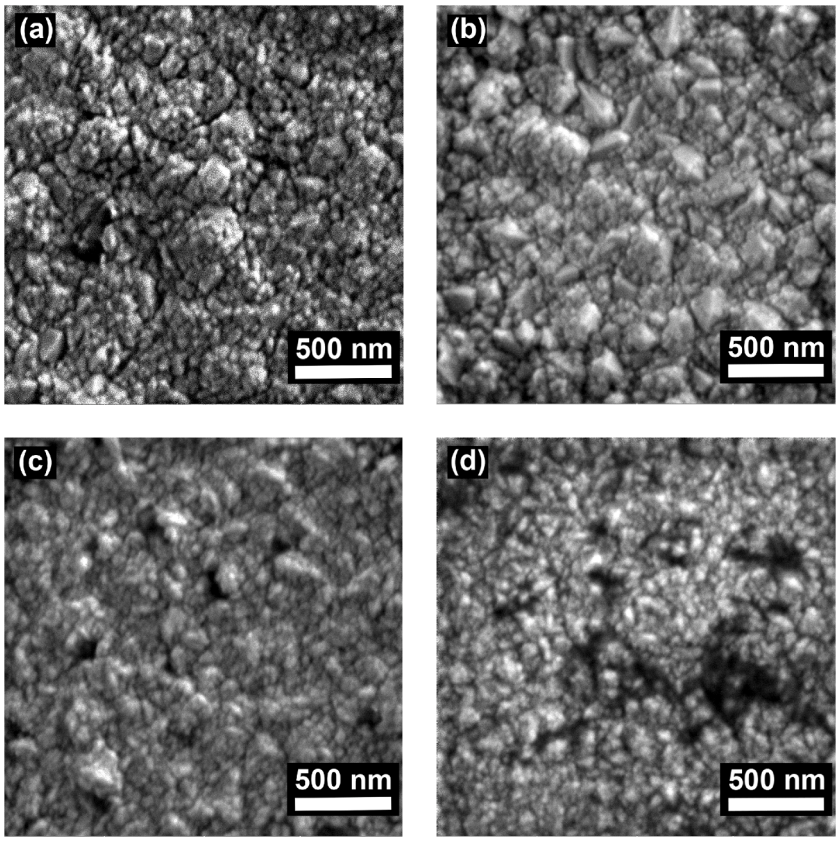

Fig. 3. SEM images depicting the surface morphologies of (a) PDD-63, (b) PDD-63-D, (c) PDD-250, and (d) PDD-1000 samples.

comparable C_{dl} of 8 μF cm^{-2} was recorded under similar conditions (in a neutral 1 mol L^{-1} Na_2SO_4 aqueous solution using the same scan rate of 100 mV s^{-1}) [26]. Interestingly, the C_{dl} values measured for PDD electrodes are comparable to those typically observed for high-quality BDD in neutral supporting electrolytes, which are generally < 10 μF cm^{-2} [3,47].

Notably, the undoped nanocrystalline diamond layer was found conductive as it enabled recording of the background currents, see Fig. S5, with a C_{dl} of 1.5 μF cm^{-2}. Even though diamond is generally considered an insulating material, (ultra)nanocrystalline CVD diamond films may exhibit some conductivity effects [48-50]. Such limited conductivity presumably originates from the presence of non-diamond (graphitic) carbon inclusions, revealed by Raman spectroscopy (see Fig. S3), and other defects in the intercrystallite boundaries [48], whose fraction in the tested undoped diamond sample is significant due to the wide presence of nano-sized grains (Fig. S4(e)).

3.3.2. *Mott-Schottky analysis*

To acquire further information on the 'active' P content present in the PDD layers, the Mott-Schottky (MS) analysis [28,51] was conducted in a 1 mol L^{-1} KCl solution using the procedure described in Section 2.4. The recorded MS plots are displayed in Fig. S6; the linear part of each plot was used to estimate P concentrations ($[P]_{MS}$), which are summarized in Table 1. A similar trend can be observed as in the case of GDOES measurements (see Section 3.1), i.e., a gradual increase in $[P]_{MS}$ corresponding to the rising $[PH_3]/[H_2]$ ratio used during the growth of the PDD layers. In addition, the PDD-63-D sample manifested approximately two orders of magnitude higher $[P]_{MS}$, in contrast to PDD-63, again confirming the ability of the dynamic gas flow mode to incorporate more phosphorus dopants into the diamond layer, compared to the static growth conditions.

Next, for all studied PDD samples, consistently lower phosphorus concentrations were recognised by the MS analysis than by the GDOES measurements ($[P]_{MS} < [P]_{GDOES}$), which indicates that not all incorporated phosphorus atoms contribute to the conductivity of the as-deposited PDD layers. Similar finding was reported in [29], where the MS analysis yielded phosphorus concentrations one order of magnitude lower than those determined by secondary ion mass spectrometry (SIMS) and energy-dispersive X-ray spectroscopy (STEM-EDX) techniques. A potential explanation for the discrepancy between phosphorus concentration values obtained by the GDOES and MS analyses could stem from oxygen chemisorption on phosphorus atoms, where oxygen, an electron-withdrawing element, interacts with phosphorus, an electron donor. This interaction, leading to the formation of P-O bonds, has been documented in P-doped sp^2-carbon materials like graphene and carbon nanotubes [52]. Additionally, phosphorus atoms might be passivated by hydrogen (abundant in the CVD chamber) and/or incorporated as hydrogenated phosphorus species within inter-grain sites [53,54], possibly rendering the phosphorus atoms inactive and non-conductive. Although the Raman spectra (shown in Fig. 2(a) and Fig. S3) indicate the incorporation of P atoms into the diamond lattice, a portion of phosphorus atoms (whether passivated or not) may, indeed, reside in the grain boundary phase and at the non-substitutional sites within the diamond grains [26,29]. In a recent study on B-doped diamond, we showed that boron atoms accumulated in the grain boundary regions are predominantly of inactive nature, as this localized enrichment did not result in enhanced electrochemical activity [55]. Phosphorus atoms in the diamond layer may exhibit comparable behaviour; however, further research is necessary to verify the presented hypotheses.

3.4. *Electrochemical characterisation with redox markers*

The electrochemical characteristics of the PDD layers were further evaluated through recording the CVs of two inorganic redox probes, specifically $[Ru(NH_3)_6]^{3+/2+}$ and $[Fe(CN)_6]^{3-/4-}$. The same set of

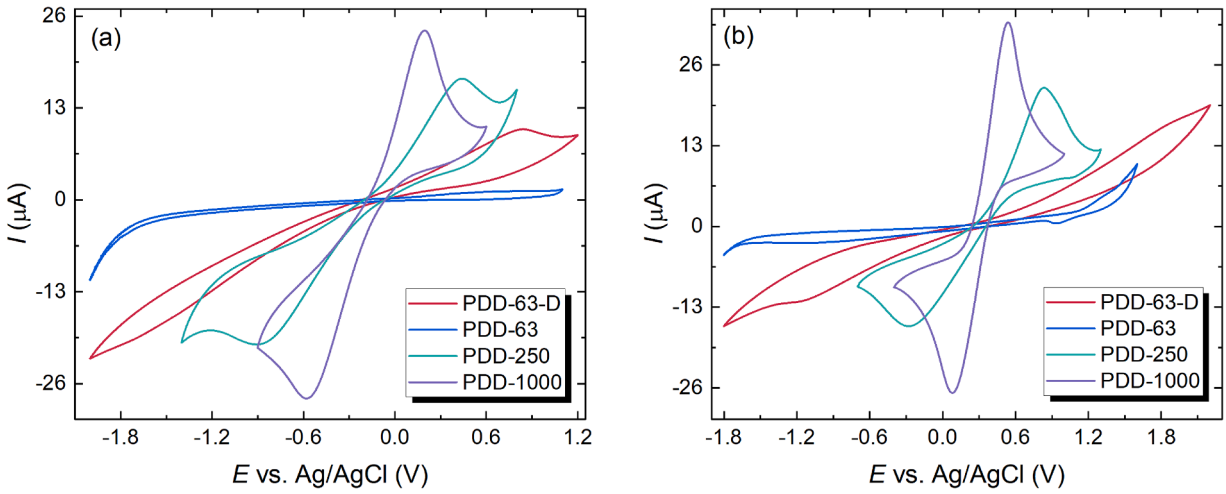

Fig. 4. Cyclic voltammograms recorded in (a) $[Ru(NH_3)_6]^{3+/2+}$ and (b) $[Fe(CN)_6]^{3-/4-}$ (both 1 mmol L^{-1} in 1 mol L^{-1} KCl) on four different PDD samples. Scan rate (ν) of 100 mV s^{-1}.

experiments was conducted on an undoped nanocrystalline diamond sample but no peaks corresponding to the redox reactions were detected. Hence, electron transfer (ET) is not promoted at this sample, despite possessing limited conductivity manifested during the measurements in a supporting electrolyte (see Section 3.3.1 and Fig. S5). Concerning the PDD layers, the nature of the recorded CV curves, displayed in Fig. 4 (a and b), largely depends on the P-doping level. Several trends can evidently be identified with increasing P content: (i) better-developed and clearly shaped voltammograms, (ii) lower oxidation and reduction potentials effectively resulting in decreased peak-to-peak separation (ΔE_p) values serving as an ET rate indicator, and (iii) higher anodic and cathodic peak currents.

Turning to the PDD samples deposited using the same $[PH_3]/[H_2]$ of 63 ppm but under different gas flow mode, the one prepared with a dynamic mode (PDD-63-D) manifested slightly improved electrochemical performance as at least ill-shaped CV curves were obtained. This could be ascribed to the redox reactions occurring at the PDD electrode | electrolyte interface. In contrast, no peaks were detected on the PDD-63 sample deposited under static gas flow mode. This implies that the selected gas flow mode affects the electrochemical behaviour of the PDD electrodes. As already observed during the GDOES analysis (see Section 3.1), the dynamic growth mode improves the efficiency of P dopants incorporation into the diamond lattice (Fig. 1). Moreover, the GDOES and MS analyses revealed fairly comparable [P] of PDD-63-D and PDD-250 samples (Table 1) but did not translate into similar electrochemical characteristics of these two electrodes. In contrast, their electrochemical performance is dramatically different as the PDD-250 sample provided well-defined pairs of redox peaks for both markers and important peak parameters could be extracted. This also holds true for the highest doped PDD-1000 electrode with even further improved electrochemical characteristics, compared to the PDD-250 electrode. Notably, this is the first time that such well-developed cyclic voltammograms of redox markers were successfully recorded on PDD electrodes without applying any pre-treatment. Mukuda et al. [28] recorded only hints of peaks corresponding to $[Ru(NH_3)_6]^{3+/2+}$ on anodically and cathodically pre-treated PDD electrode, which was ascribed to its semi-conductive nature ($[P]_{MS}$ of 7.4 × 10^{18} cm^{-3}). Interestingly, as-deposited and heavily P-doped nanocrystalline diamond with claimed $[P]_{SIMS}$ of 5 × 10^{20} cm^{-3} was not able to detect any peaks of $[Fe(CN)_6]^{3-/4-}$ redox marker in [26], and thermal annealing (vacuum, 800 °C, 7 h), leading to graphitisation of the electrode surface, was required to improve its electrochemical behaviour.

As can be further seen in Fig. 4(a, b), the acquired CV curves on PDD-250 and PDD-1000 electrodes have (quasi)reversible character as ΔE_p of 1.29 V (PDD-250) and 0.79 V (PDD-1000), and 1.08 V (PDD-250) and 0.45 V (PDD-1000) were obtained for $[Ru(NH_3)_6]^{3+/2+}$ and $[Fe(CN)_6]^{3-/4-}$, respectively (see also Table 2). Thus, faster ET rate was recognized for the latter redox probe. In contrast, for BDD electrodes, a different trend is usually observed. Smaller ΔE_p values are noted for $[Ru(NH_3)_6]^{3+/2+}$, often approaching 59 mV, indicative of a reversible single-electron transfer if the BDD electrode is sufficiently doped, due to its outer-sphere reaction character [3,56]. Conversely, larger ΔE_p values and hindered ET rates are typically seen for $[Fe(CN)_6]^{3-/4-}$, a response that is very sensitive to the surface characteristics of BDD electrodes, particularly the surface (H- vs. O-) termination [3,5]. The differences in heterogeneous ET kinetics and the associated ΔE_p values for redox markers on PDD and BDD electrodes can likely be attributed to their distinct types of conductivity. PDD exhibits n-type conductivity, which arises from the presence of additional electrons (negative charge carriers) moving in the conduction band, with phosphorus atoms acting as donors [28]. In contrast, BDD displays p-type conductivity, facilitated by the presence of holes (positive charge carriers) moving in the valence band, where boron atoms serve as acceptors [3,28].

Table 2
Parameters of redox responses of $[Ru(NH_3)_6]^{3+/2+}$, $[Fe(CN)_6]^{3-/4-}$, dopamine (DA) and ascorbic acid (AA) obtained from CV measurements (at the scan rate of 100 mV s^{-1}) on the PDD electrodes.

PDD electrode	PDD-63-D	PDD-250	PDD-1000
ΔE_p - $[Ru(NH_3)_6]^{3+/2+}$ (V)	(E_{pA} ~ +0.84) [a]	1.29	0.75
ΔE_p - $[Fe(CN)_6]^{3-/4-}$ (V)	> 3.0	1.08	0.45
$E_{pA1,\ DA}$ (V)	+1.25	+0.69	+0.55
$I_{pA1,\ DA}$ (μA)	4.2	6.2	7.3
ΔE_p – DA/*o*-DQ (V)	- [a]	0.72	0.53
$E_{p,\ AA}$ (V)	+1.70	+1.02	+0.94
$I_{p,\ AA}$ (μA)	3.8	5.6	6.3

[a] Only the anodic (oxidation) peak was recognized and evaluated in the CVs.

In addition, the PDD-250 and PDD-1000 samples were subjected to scan rate studies in the presence of both redox markers; recorded voltammograms are depicted in Fig. 5. The extracted ΔE_p values for each scan rate are shown in Fig. 5(e, f). These graphs clearly revealed that smaller ΔE_p, and thus facilitated rate of ET kinetics for both markers is recognized on the PDD-1000 electrode which can be ascribed to its higher P-doping level (Table 1). In the case of both PDD samples, the linear dependence of the cathodic peak currents on the square root of the scan rate was also evaluated for both markers (with the coefficient of determination R^2 in the range of 0.977 – 0.997), indicating diffusion-controlled redox reaction (see the insets in Fig. 5(a-d)).

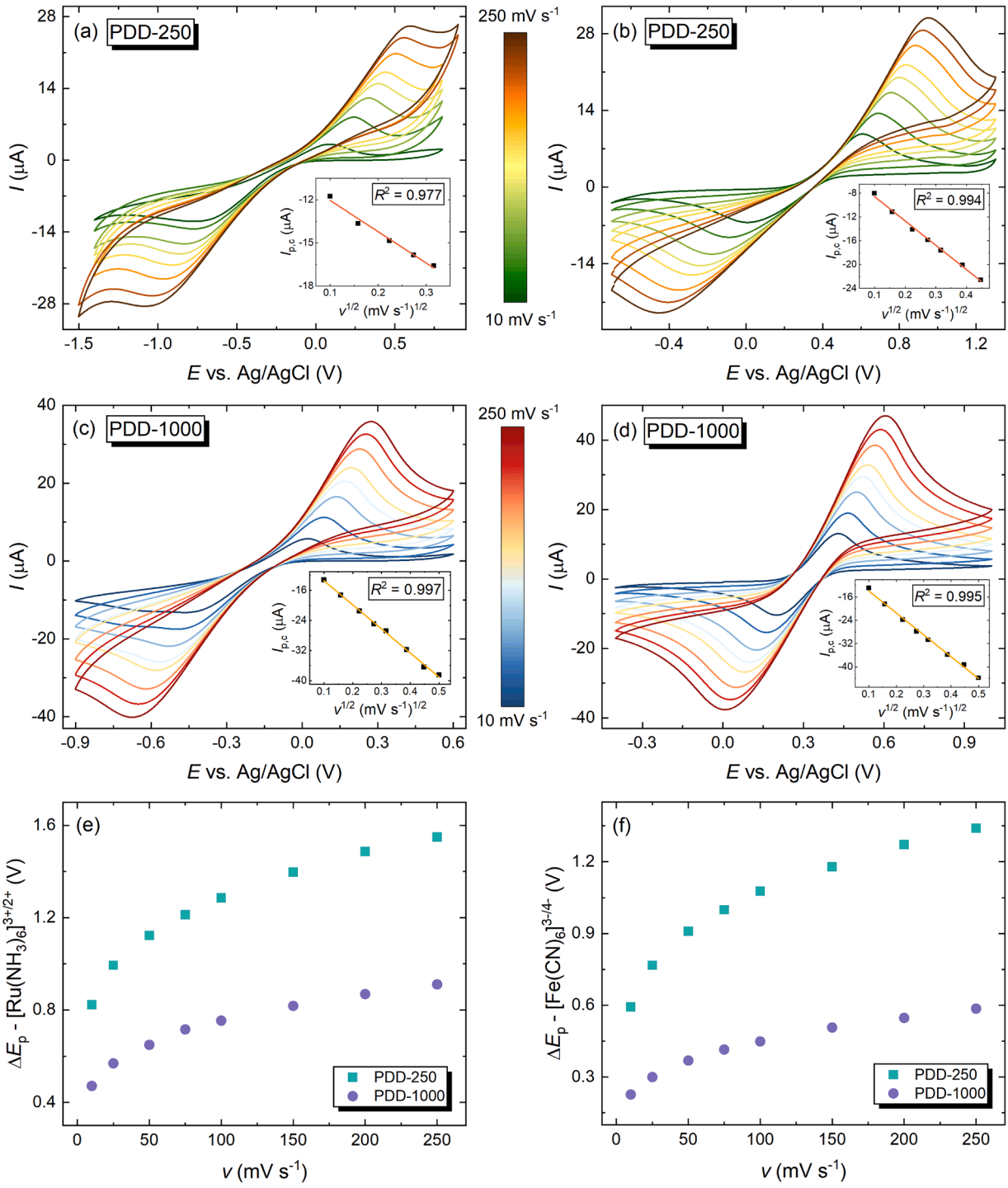

Fig. 5. Cyclic voltammograms recorded at different scan rates in (a, c) $[Ru(NH_3)_6]^{3+/2+}$ and (b, d) $[Fe(CN)_6]^{3-/4-}$ (both 1 mmol L^{-1} in 1 mol L^{-1} KCl) on the (a, b) PDD-250 and (c, d) PDD-1000 electrodes. The insets show linear dependence of the cathodic peak current ($I_{p,C}$) on the square root of the scan rate ($v^{1/2}$) with corresponding coefficient of determination (R^2). (e, f) The dependence of peak-to-peak separation (ΔE_p) values of (e) $[Ru(NH_3)_6]^{3+/2+}$ and (f) $[Fe(CN)_6]^{3-/4-}$ on the scan rate (v) acquired on the PDD-250 and PDD-1000 electrodes.

3.5. Cyclic voltammetry of organic molecules

Finally, the as-deposited PDD samples were subjected to CV experiments in the presence of two organic analytes, dopamine and ascorbic acid, in order to further explore their electrochemical performance and ability to provide responses for structurally more complex compounds whose redox reactions involve more than a single electron [57,58]. Dopamine and ascorbic acid were selected because their redox reactions are well-defined and proceed through inner-sphere ET mechanisms, which make them sensitive to the surface and electronic characteristics of BDD materials [56,58-60], and presumably also PDD electrodes. Indeed, as clearly depicted in Fig. 6, the variously doped PDD samples provided significantly different electrochemical responses towards the two organic analytes, which can be associated with different phosphorus content. Similarly to previous experiments with inorganic redox markers (see Section 3.4), the PDD-63 sample failed to provide any distinguishable signals for dopamine and ascorbic acid, whereas on the PDD-63-D somewhat improved responses were recognized, however, still far

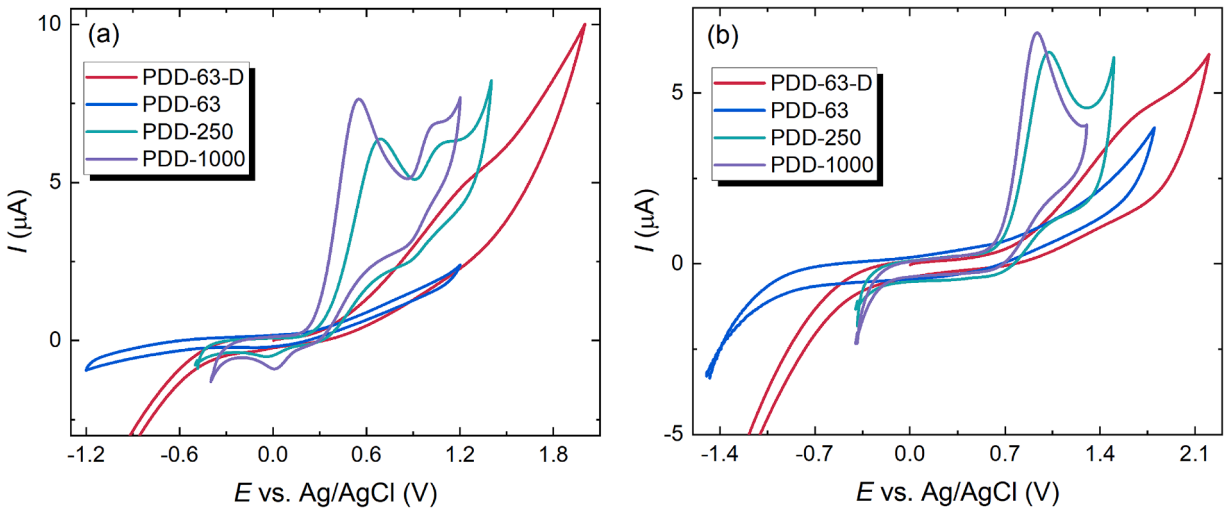

Fig. 6. Cyclic voltammograms of (a) 100 μmol L^{-1} dopamine in 10 mmol L^{-1} PBS of pH 7.4 and (b) 100 μmol L^{-1} ascorbic acid in 0.1 mol L^{-1} H_2SO_4 recorded on four different PDD samples.

from satisfactory. Again, the best developed peaks were recognized on PDD-250 and PDD-1000 electrodes. Peak potentials (E_p) and currents (I_p) were determined, and the values obtained, tabulated in Table 2, confirmed the trend of decreasing E_p and increasing I_p with increasing P-doping. Notably, such effect of P-doping on the electrochemical behaviour of PDD electrodes is recognized for the first time. Previously, similar observations have been made for P-doped tetrahedral amorphous carbon electrodes [61] and diamond electrodes doped with boron, e.g., in [6,13,60,62].

Further, Fig. 6(a) depicts the CVs of dopamine. On the hPDD electrodes, a (quasi)reversible dopamine/dopamine-*o*-quinone (DA/*o*-DQ) redox pair can be clearly recognized in a potential range from −0.30 to +0.70 V. Consequently, ΔE_p could be evaluated as 0.72 V and 0.53 V for PDD-250 and PDD-1000 electrodes, respectively. This again proves facilitated dopamine ET kinetics on the latter PDD sample. Interestingly, the ΔE_p values obtained on as-deposited PDD electrodes are fairly comparable to the ones obtained for dopamine on highly doped but oxidized BDD electrodes (ΔE_p of 0.50 – 0.66 V [63,64]). Dopamine-*o*-quinone can undergo a spontaneous ring closure resulting in the formation of leucodopaminechrome, which may be further oxidized into dopaminechrome [65]. This is manifested in the CVs (shown in Fig. 6(a)) as the second developed oxidation peak at ~ +1.0 V. In contrast, the oxidation reaction of ascorbic acid has typically irreversible character, thus no reduction peak was detected in the recorded CVs, displayed in Fig. 6(b). Markedly, the obtained anodic peak potential ($E_{p,\ AA}$) values of +1.02 V and +0.94 V on PDD-250 and PDD-1000, respectively, are, again, roughly equivalent to the $E_{p,\ AA}$ previously obtained on both hydrogen-terminated ($E_{p,\ AA}$ of +0.80 ± 0.01 V) [56,66,67] and oxygen-terminated BDD electrodes ($E_{p,\ AA}$ > +1.2 V) [57,66]. These observations highlight the efficiency of hPDD electrodes in the electrochemical detection of dopamine and ascorbic acid, illustrating their performance comparable to that of oxidized BDD electrodes. This further supports the potential applicability of PDD in diverse electrochemical sensor applications, similarly to the established uses of BDD materials.

All in all, the as-grown, heavily P-doped diamond electrodes successfully enabled, first time ever, the recording of well-defined voltammetric signals of both inorganic redox probes and more complex organic compounds. This clearly confirms their potential for applications in electroanalysis and sensor development, broadening the scope of PDD utilisation. Previously recognised as a promising electrode material for, e.g., supercapacitor devices [26] and carbon dioxide reduction [30], this research further extends the newly emerging, versatile applications of PDD materials.

4. Conclusions

We comprehensively investigated the impact of phosphorus doping levels and the gas flow mode (static vs. dynamic) on the properties of as-grown, polycrystalline PDD samples. Under static flow mode, increasing the $[PH_3]/[H_2]$ ratio in the gas phase enhanced phosphorus incorporation in the deposited PDD layers, as confirmed by GDOES analysis, while concurrently their thicknesses decreased due to reduced growth rates. In addition, SEM revealed a gradual decrease in the diamond grain size with elevated $[PH_3]/[H_2]$ ratios, which was also coupled with an increase in non-diamond carbon components, as evidenced by the recorded Raman spectra. Dynamic gas flow, used to prepare the PDD-63-D sample, facilitated an efficient growth process, resulting in a higher phosphorus level, a larger grain size, a faster growth rate, and a reduction in the consumption of the phosphine gas precursor, in contrast to the PDD-63 deposited under static flow. This suggests the possibility of precisely controlling phosphorus content and microstructure of the layer by adjusting dynamic gas flow conditions for advanced electrochemical devices.

This study marks successful preparation of hPDD electrodes, which, for the first time, provided distinct voltammetric signals for both simple inorganic redox markers and complex organic molecules requiring multi-electron transfer processes. The variation in phosphorus levels within the PDD layers significantly influenced their electrochemical behaviour: enhanced cyclic voltammograms were recorded with increased phosphorus doping as evidenced by more defined shapes, lower potentials (and associated ΔE_p values), and higher currents. Despite MS analysis indicating that not all phosphorus atoms contribute to conductivity, with some possibly being inactive due to oxygen chemisorption, hydrogen passivation or location within inter-grain regions and/or non-substitutional sites, these initial findings pave the way for novel applications of as-grown hPDD electrodes in the previously unexplored areas of electroanalysis and sensor development. Since the incorporation of phosphorus atoms into the diamond structure is expected to enhance its hydrophilicity and act as electron donors within the sp^3 carbon frameworks, PDD electrodes may exhibit a notable affinity for basic and/or positively charged compounds. As a result, PDD electrodes may show promising electrochemical behaviour in detecting heavy metal ions and reducible aromatic organic molecules such as those containing, e.g., primary and secondary amine groups.

CRediT authorship contribution statement

Simona Baluchová: Writing – review & editing, Writing – original draft, Visualization, Investigation, Formal analysis, Data curation, Conceptualization. **Kil-dong Sung:** Writing – review & editing, Writing – original draft, Visualization, Investigation, Formal analysis, Data curation, Conceptualization. **Zdeněk Weiss:** Writing – review & editing, Investigation, Formal analysis. **Jaromír Kopeček:** Writing – review & editing, Visualization, Investigation. **Ladislav Fekete:** Writing – review & editing, Investigation. **Josephus G. Buijnsters:** Writing – review & editing, Supervision, Conceptualization. **Vincent Mortet:** Writing – review & editing, Supervision, Project administration, Funding acquisition, Conceptualization.

Declaration of competing interest

The authors declare that they have no known competing financial interests or personal relationships that could have appeared to influence the work reported in this paper.

Data availability

Data will be made available on request.

Acknowledgements

This work was financially supported by the Czech Science Foundation (project no. GACR 21–03538S) and the CzechNanoLab Research Infrastructure financed by the Czech Ministry of Education, Youth and Sports (project no. LM2023051).

Supplementary materials

Supplementary material associated with this article can be found, in the online version, at doi:10.1016/j.electacta.2024.144696.

References

[1] C.J.H. Wort, R.S. Balmer, Diamond as an electronic material, Mater. Today 11 (2008) 22–28.
[2] R.S. Balmer, J.R. Brandon, S.L. Clewes, H.K. Dhillon, J.M. Dodson, I. Friel, P. N. Inglis, T.D. Madgwick, M.L. Markham, T.P. Mollart, N. Perkins, G.A. Scarsbrook, D.J. Twitchen, A.J. Whitehead, J.J. Wilman, S.M. Woollard, Chemical vapour deposition synthetic diamond: materials, technology and applications, J. Condens. Matter Phys. 21 (2009) 364221.
[3] J.V. Macpherson, A practical guide to using boron doped diamond in electrochemical research, Phys. Chem. Chem. Phys. 17 (2015) 2935–2949.
[4] U.F.S. D'Haenens-Johansson, J.E. Butler, A.N. Katrusha, Synthesis of diamonds and their identification, Rev. Mineral. Geochem. 88 (2022) 689–753.
[5] N. Yang, S. Yu, J.V. Macpherson, Y. Einaga, H. Zhao, G. Zhao, G.M. Swain, X. Jiang, Conductive diamond: synthesis, properties, and electrochemical applications, Chem. Soc. Rev. 48 (2019) 157–204.
[6] S. Baluchová, A. Daňhel, H. Dejmková, V. Ostatná, M. Fojta, K. Schwarzová-Pecková, Recent progress in the applications of boron doped diamond electrodes in electroanalysis of organic compounds and biomolecules – A review, Anal. Chim. Acta 1077 (2019) 30–66.
[7] T. Kondo, Recent electroanalytical applications of boron-doped diamond electrodes, Curr. Opin. Electrochem. 32 (2022) 100891.
[8] A.V. Karim, P.V. Nidheesh, M.A. Oturan, Boron-doped diamond electrodes for the mineralization of organic pollutants in the real wastewater, Curr. Opin. Electrochem. 30 (2021) 100855.
[9] D. Suresh Babu, J.M.C. Mol, J.G. Buijnsters, Experimental insights into anodic oxidation of hexafluoropropylene oxide dimer acid (GenX) on boron-doped diamond anodes, Chemosphere 288 (2022) 132417.
[10] S. Lips, S.R. Waldvogel, Use of boron-doped diamond electrodes in electro-organic synthesis, ChemElectroChem 6 (2019) 1649–1660.
[11] C. Guo, J. Zheng, H. Deng, P. Shi, G. Zhao, Photoelectrocatalytic interface of boron-doped diamond: modification, functionalization and environmental applications, Carbon 175 (2021) 454–466.
[12] J. Raymakers, K. Haenen, W. Maes, Diamond surface functionalization: from gemstone to photoelectrochemical applications, J. Mater. Chem. C 7 (2019) 10134–10165.
[13] K. Schwarzová-Pecková, J. Vosáhlová, J. Barek, I. Šloufová, E. Pavlova, V. Petrák, J. Zavázalová, Influence of boron content on the morphological, spectral, and electroanalytical characteristics of anodically oxidized boron-doped diamond electrodes, Electrochim. Acta 243 (2017) 170–182.
[14] R. Šelešovská, B. Kränková, M. Štěpánková, P. Martinková, L. Janíková, J. Chýlková, M. Vojs, Influence of boron content on electrochemical properties of boron-doped diamond electrodes and their utilization for leucovorin determination, J. Electroanal. Chem. 821 (2018) 2–9.
[15] P. Kuang, K. Natsui, C. Feng, Y. Einaga, Electrochemical reduction of nitrate on boron-doped diamond electrodes: effects of surface termination and boron-doping level, Chemosphere 251 (2020) 126364.
[16] I.M.D. Gonzaga, A. Moratalla, K.I.B. Eguiluz, G.R. Salazar-Banda, P. Cañizares, M. A. Rodrigo, C. Saez, Influence of the doping level of boron-doped diamond anodes on the removal of penicillin G from urine matrixes, Sci. Total Environ. 736 (2020) 139536.
[17] Ľ. Švorc, D. Jambrec, M. Vojs, S. Barwe, J. Clausmeyer, P. Michniak, M. Marton, W. Schuhmann, Doping level of boron-doped diamond electrodes controls the grafting density of functional groups for DNA assays, ACS Appl. Mater. Interfaces 7 (2015) 18949–18956.
[18] A.F. Azevedo, M.R. Baldan, N.G. Ferreira, Doping level influence on chemical surface of diamond electrodes, J. Phys. Chem. Solids 74 (2013) 599–604.
[19] M.N.R. Ashfold, J.P. Goss, B.L. Green, P.W. May, M.E. Newton, C.V. Peaker, Nitrogen in diamond, Chem. Rev. 120 (2020) 5745–5794.
[20] E. Janitz, K. Herb, L.A. Völker, W.S. Huxter, C.L. Degen, J.M. Abendroth, Diamond surface engineering for molecular sensing with nitrogen—vacancy centers, J. Mater. Chem. C 10 (2022) 13533–13569.
[21] W. Janssen, S. Turner, G. Sakr, F. Jomard, J. Barjon, G. Degutis, Y.-G. Lu, J. D'Haen, A. Hardy, M.V. Bael, J. Verbeeck, G.V. Tendeloo, K. Haenen, Substitutional phosphorus incorporation in nanocrystalline CVD diamond thin films, Phys. Status Solidi Rapid Res. Lett. 8 (2014) 705–709.
[22] H. Kato, H. Umezawa, N. Tokuda, D. Takeuchi, H. Okushi, S. Yamasaki, Low specific contact resistance of heavily phosphorus-doped diamond film, Appl. Phys. Lett. 93 (2008) 202103.
[23] T.A. Grotjohn, D.T. Tran, M.K. Yaran, S.N. Demlow, T. Schuelke, Heavy phosphorus doping by epitaxial growth on the (111) diamond surface, Diam. Relat. Mater. 44 (2014) 129–133.
[24] Y. Katamune, A. Izumi, K. Ichikawa, S. Koizumi, Heavy phosphorus doping of diamond by hot-filament chemical vapor deposition, Diam. Relat. Mater. 134 (2023) 109789.
[25] H. Kato, D. Takeuchi, M. Ogura, T. Yamada, M. Kataoka, Y. Kimura, S. Sobue, C. E. Nebel, S. Yamasaki, Heavily phosphorus-doped nano-crystalline diamond electrode for thermionic emission application, Diam. Relat. Mater. 63 (2016) 165–168.
[26] S. Yu, J. Xu, H. Kato, N. Yang, A. Schulte, H. Schönherr, X. Jiang, Phosphorus-doped nanocrystalline diamond for supercapacitor application, ChemElectroChem 6 (2019) 1088–1093.
[27] N. Lambert, Z. Weiss, L. Klimša, J. Kopeček, Z. Gedeonová, P. Hubík, V. Mortet, Highly phosphorus-doped polycrystalline diamond growth and properties, Diam. Relat. Mater. 125 (2022) 108964.
[28] Y. Mukuda, T. Watanabe, A. Ueda, Y. Nishibayashi, Y. Einaga, Electrochemical properties of phosphorus doped diamond, Electrochim. Acta 179 (2015) 599–603.
[29] Z. Vlčková Živcová, O. Frank, S. Drijkoningen, K. Haenen, V. Mortet, L. Kavan, n-Type phosphorus-doped nanocrystalline diamond: electrochemical and in situ Raman spectroelectrochemical study, RSC Adv. 6 (2016) 51387–51393.
[30] H. Naragino, Y. Saitoh, K. Honda, Electrochemical reduction of carbon dioxide in an aqueous solution using phosphorus-doped polycrystalline diamond electrodes, Electrochem. Commun. 134 (2022) 107164.
[31] M.-A. Pinault-Thaury, I. Stenger, R. Gillet, S. Temgoua, E. Chikoidze, Y. Dumont, F. Jomard, T. Kociniewski, J. Barjon, Attractive electron mobility in (113) n-type phosphorus-doped homoepitaxial diamond, Carbon N Y 175 (2021) 254–258.
[32] M.-A. Pinault-Thaury, S. Temgoua, R. Gillet, H. Bensalah, I. Stenger, F. Jomard, R. Issaoui, J. Barjon, Phosphorus-doped (113) CVD diamond: a breakthrough towards bipolar diamond devices, Appl. Phys. Lett. 114 (2019) 112106.
[33] Y.-J. Lu, C.-N. Lin, C.-X. Shan, Optoelectronic diamond: growth, properties, and photodetection applications, Adv. Opt. Mater. 6 (2018) 1800359.
[34] M. Liao, H. Sun, S. Koizumi, High-temperature and high-electron mobility metal-oxide-semiconductor field-effect transistors based on n-type diamond, Adv. Sci. (2024) 2306013.
[35] V. Mortet, A. Taylor, M. Davydova, M. Lamač, N. Lambert, I. Elantyev, J. Lorinčík, D. Troadec, M. Vronka, S. Potocký, Effect of pulsed methane gas flow on the incorporation of phosphorous in diamond, Diam. Relat. Mater. 124 (2022) 108928.
[36] Z. Weiss, Calibration methods in glow discharge optical emission spectroscopy: a tutorial review, J. Anal. At. Spectrom. 30 (2015) 1038–1049.
[37] Z. Weiss, P. Ashcheulov, N. Lambert, A. Taylor, J. Lorincik, K.-d. Sung, M. Davydova, V. Mortet, Analysis of boron- and phosphorus-doped diamond layers by glow discharge optical emission spectroscopy in argon and neon, Vacuum 210 (2023) 111890.
[38] Z. Weiss, Propagation of uncertainty in multi-matrix analysis by GD-OES, J. Anal. At. Spectrom. 16 (2001) 1275–1282.
[39] M.A. Lobaev, D.B. Radishev, A.M. Gorbachev, A.L. Vikharev, M.N. Drozdov, Investigation of microwave plasma during diamond doping by phosphorus using optical emission spectroscopy, Phys. Status Solidi A 216 (2019) 1900234.
[40] N. Lambert, K.-D. Sung, V. Mortet, Optical emission spectroscopy analysis of microwave plasma-enhanced chemical vapor deposition systems dynamic gas response, Phys. Status Solidi A 220 (2023) 2200322.

[41] F. Klauser, D. Steinmüller-Nethl, R. Kaindl, E. Bertel, N. Memmel, Raman studies of nano- and ultra-nanocrystalline diamond films grown by hot-filament CVD, Chem. Vap. Depos. 16 (2010) 127–135.
[42] V. Mortet, Z.V. Živcová, A. Taylor, M. Davydová, O. Frank, P. Hubík, J. Lorincik, M. Aleshin, Determination of atomic boron concentration in heavily boron-doped diamond by Raman spectroscopy, Diam. Relat. Mater. 93 (2019) 54–58.
[43] V. Mortet, I. Gregora, A. Taylor, N. Lambert, P. Ashcheulov, Z. Gedeonova, P. Hubik, New perspectives for heavily boron-doped diamond Raman spectrum analysis, Carbon 168 (2020) 319–327.
[44] N. Habka, J. Barjon, A. Lazea, K. Haenen, Stress in (110)-textured phosphorus-doped polycrystalline diamond studied by Raman and cathodoluminescence spectroscopies, J. Appl. Phys. 107 (2010) 103531.
[45] M. Matsuoka, Y. Tsuchida, N. Ohtani, T. Yamada, S. Koizumi, S. Shikata, Polarized Raman spectroscopy of phosphorous doped diamond films, Diam. Relat. Mater. 114 (2021) 108283.
[46] T. Yokoya, K. Terashima, A. Takeda, T. Fukura, H. Fujiwara, T. Muro, T. Kinoshita, H. Kato, S. Yamasaki, T. Oguchi, T. Wakita, Y. Muraoka, T. Matsushita, Asymmetric phosphorus incorporation in homoepitaxial P-doped (111) diamond revealed by photoelectron holography, Nano Lett. 19 (2019) 5915–5919.
[47] L.A. Hutton, J.G. Iacobini, E. Bitziou, R.B. Channon, M.E. Newton, J. V. Macpherson, Examination of the factors affecting the electrochemical performance of oxygen-terminated polycrystalline boron-doped diamond electrodes, Anal. Chem. 85 (2013) 7230–7240.
[48] K.B. Holt, C. Ziegler, J. Zang, J. Hu, J.S. Foord, Scanning electrochemical microscopy studies of redox processes at undoped nanodiamond surfaces, J. Phys. Chem. C 113 (2009) 2761–2770.
[49] Y.V. Pleskov, M.D. Krotova, V.V. Elkin, V.G. Ralchenko, A.V. Saveliev, S. M. Pimenov, P.Y. Lim, n-Type nitrogenated nanocrystalline diamond thin-film electrodes: the effect of the nitrogenation on electrochemical properties, Electrochim. Acta 52 (2007) 5470–5478.
[50] N.G. Ferreira, A.F. Azevedo, A.F. Beloto, M. Amaral, F.A. Almeida, F.J. Oliveira, R. F. Silva, Nanodiamond films growth on porous silicon substrates for electrochemical applications, Diam. Relat. Mater. 14 (2005) 441–445.
[51] Z.V. Živcová, V. Petrák, O. Frank, L. Kavan, Electrochemical impedance spectroscopy of polycrystalline boron doped diamond layers with hydrogen and oxygen terminated surface, Diam. Relat. Mater. 55 (2015) 70–76.
[52] H.-m. Wang, H.-x. Wang, Y. Chen, Y.-j. Liu, J.-x. Zhao, Q.-h. Cai, X.-z. Wang, Phosphorus-doped graphene and (8, 0) carbon nanotube: structural, electronic, magnetic properties, and chemical reactivity, Appl. Surf. Sci. 273 (2013) 302–309.
[53] S. Koizumi, M. Kamo, Y. Sato, H. Ozaki, T. Inuzuka, Growth and characterization of phosphorous doped {111} homoepitaxial diamond thin films, Appl. Phys. Lett. 71 (1997) 1065–1067.
[54] E.B. Lombardi, A. Mainwood, K. Osuch, Interaction of hydrogen with boron, phosphorus, and sulfur in diamond, Phys. Rev. B 70 (2004) 205201.
[55] Z. Liu, S. Baluchová, Z. Li, Y. Gonzalez-Garcia, C.E. Hall, J.G. Buijnsters, Unravelling microstructure-electroactivity relationships in free-standing polycrystalline boron-doped diamond: a mapping study, Acta Mater. 266 (2024) 119671.
[56] M.C. Granger, M. Witek, J. Xu, J. Wang, M. Hupert, A. Hanks, M.D. Koppang, J. E. Butler, G. Lucazeau, M. Mermoux, J.W. Strojek, G.M. Swain, Standard electrochemical behavior of high-quality, boron-doped polycrystalline diamond thin-film electrodes, Anal. Chem. 72 (2000) 3793–3804.
[57] Y. Qi, H. Long, L. Ma, Q. Wei, S. Li, Z. Yu, J. Hu, P. Liu, Y. Wang, L. Meng, Enhanced selectivity of boron doped diamond electrodes for the detection of dopamine and ascorbic acid by increasing the film thickness, Appl. Surf. Sci. 390 (2016) 882–889.
[58] S. Baluchová, M. Brycht, A. Taylor, V. Mortet, J. Krůšek, I. Dittert, S. Sedláková, L. Klimša, J. Kopeček, K. Schwarzová-Pecková, Enhancing electroanalytical performance of porous boron-doped diamond electrodes by increasing thickness for dopamine detection, Anal. Chim. Acta 1182 (2021) 338949.
[59] J.A. Bennett, J. Wang, Y. Show, G.M. Swain, Effect of sp2-bonded nondiamond carbon impurity on the response of boron-doped polycrystalline diamond thin-film electrodes, J. Electrochem. Soc. 151 (2004) E306.
[60] S. Baluchová, A. Taylor, V. Mortet, S. Sedláková, L. Klimša, J. Kopeček, O. Hák, K. Schwarzová-Pecková, Porous boron doped diamond for dopamine sensing: effect of boron doping level on morphology and electrochemical performance, Electrochim. Acta 327 (2019) 135025.
[61] A. Liu, J. Zhu, J. Han, H. Wu, W. Gao, Influence of phosphorus doping level and acid pretreatment on the voltammetric behavior of phosphorus incorporated tetrahedral amorphous carbon film electrodes, Electroanalysis 19 (2007) 1773–1778.
[62] M. Zelenský, J. Fischer, S. Baluchová, L. Klimša, J. Kopeček, M. Vondráček, L. Fekete, J. Eidenschink, F.M. Matysik, S. Mandal, O.A. Williams, M. Hromadová, V. Mortet, K. Schwarzová-Pecková, A. Taylor, Chem-mechanical polishing influenced morphology, spectral and electrochemical characteristics of boron doped diamond, Carbon 203 (2023) 363–376.
[63] R. Trouillon, Y. Einaga, M.A.M. Gijs, Cathodic pretreatment improves the resistance of boron-doped diamond electrodes to dopamine fouling, Electrochem. Commun. 47 (2014) 92–95.
[64] L. Jiang, G.W. Nelson, J. Abda, J.S. Foord, Novel modifications to carbon-based electrodes to improve the electrochemical detection of dopamine, ACS Appl. Mater. Interfaces 8 (2016) 28338–28348.
[65] J. Breczko, M.E. Plonska-Brzezinska, L. Echegoyen, Electrochemical oxidation and determination of dopamine in the presence of uric and ascorbic acids using a carbon nano-onion and poly(diallyldimethylammonium chloride) composite, Electrochim. Acta 72 (2012) 61–67.
[66] D.A. Tryk, H. Tachibana, H. Inoue, A. Fujishima, Boron-doped diamond electrodes: the role of surface termination in the oxidation of dopamine and ascorbic acid, Diam. Relat. Mater. 16 (2007) 881–887.
[67] Z. Liu, S. Baluchová, B. Brocken, E. Ahmed, P. Pobedinskas, K. Haenen, J. G. Buijnsters, Inkjet printing-manufactured boron-doped diamond chip electrodes for electrochemical sensing purposes, ACS Appl. Mater. Interfaces 15 (2023) 39915–39925.